

Multi-season optical modulation phased with the orbit of the super-Earth 55 Cnc e

S. Sulis¹, D. Dragomir^{2,3}, M. Lendl^{1,4}, V. Bourrier⁴, B. O. Demory⁵, L. Fossati¹, P. E. Cubillos¹, D. B. Guenther⁶, S. R. Kane⁷, R. Kuschnig⁸, J. M. Matthews⁹, A. F. J. Moffat¹⁰, J. F. Rowe¹¹, D. Sasselov¹², W. W. Weiss⁸, and J. N. Winn¹³

¹ Space Research Institute, Austrian Academy of Sciences, Schmiedlstraße 6, 8042 Graz, Austria
e-mail: sophia.sulis@oeaw.ac.at

² Department of Physics and Kavli Institute for Astrophysics and Space Research, Massachusetts Institute of Technology, Cambridge, MA 02139, USA

³ Department of Physics and Astronomy, University of New Mexico, Albuquerque, NM, USA

⁴ Observatoire de l'Université de Genève, 51 chemin des Maillettes, 1290 Sauverny, Switzerland

⁵ University of Bern, Center for Space and Habitability, Sidlerstraße 5, CH-3012 Bern, Switzerland

⁶ Institute for Computational Astrophysics, Department of Astronomy and Physics, Saint Mary's University, Halifax, NS B3H 3C3, Canada

⁷ Department of Earth and Planetary Sciences, University of California, Riverside, CA 92521, USA

⁸ Institut für Astronomie, Universität Wien Türkenschanzstrasse 17, A-1180 Wien, Austria

⁹ Department of Physics and Astronomy, University of British Columbia, 6224 Agricultural Road, Vancouver, BC V6T 1Z1, Canada

¹⁰ Observatoire Astronomique du Mont Mégantic, Département de Physique, Université de Montréal C. P. 6128, Succursale: Centre-Ville, Montréal, QC H3C 3J7, Canada

¹¹ NASA-Ames Research Park, Mail Stop 244-30, Moffett Field, CA 94035-1000;

¹² Harvard-Smithsonian Center for Astrophysics, 60 Garden Street, Cambridge, MA 102138

¹³ Department of Astrophysical Sciences, Princeton University, 4 Ivy Lane, Princeton, NJ 08544, USA

Received XX, 2019; accepted XX, 2019

ABSTRACT

Context. 55 Cnc e is a transiting super-Earth orbiting a solar-like star with an orbital period of ~ 17.7 hours. In 2011, using the Microvariability and Oscillations in Stars (MOST) space telescope, a quasi-sinusoidal modulation in flux was detected with the same period as the planetary orbit. The amplitude of this modulation was too large to be explained as the change in light reflected or emitted by the planet.

Aims. The MOST telescope continued to observe 55 Cnc e for a few weeks per year over five years (from 2011 to 2015), covering 143 individual transits. This paper presents the analysis of the observed phase modulation throughout these observations and a search for the secondary eclipse of the planet.

Methods. The most important source of systematic noise in MOST data is due to stray-light reflected from the Earth, which is modulated with both the orbital period of the satellite (101.4 minutes) and the Earth's rotation period. We present a new technique to deal with this source of noise, which we combined with standard detrending procedures for MOST data. We then performed Markov Chain Monte Carlo analyses of the detrended light curves, modeling the planetary transit and phase modulation.

Results. We find phase modulations similar to those seen in 2011 in most of the subsequent years; however, the amplitude and phase of maximum light are seen to vary, from year to year, from 113 to 28 ppm and from 0.1 to 3.8 rad. The secondary eclipse is not detected, but we constrain the geometric albedo of the planet to less than 0.47 (2σ).

Conclusions. While we cannot identify a single origin of the observed optical modulation, we propose a few possible scenarios. Those include star-planet interaction, such as coronal rains and spots rotating with the motion of the planet along its orbit, or the presence of a transiting circumstellar torus of dust. However, a detailed interpretation of these observations is limited by their photometric precision. Additional observations at optical wavelengths could measure the variations at higher precision, contribute to uncovering the underlying physical processes, and measure or improve the upper limit on the albedo of the planet.

Key words. < Planetary systems – Techniques: photometric – Stars: individual: 55 Cancri >

1. Introduction

Though super-Earths as a category of exoplanets have been discussed for nearly a decade, the nature and origins of these planets are diverse (Rogers et al. 2011; Hansen & Murray 2012; Mordasini et al. 2012; Chiang & Laughlin 2013; Batygin & Laughlin 2015; Dorn et al. 2018). A wide range of compositions are possible for these planets, whose mass and size lie between those of the Earth and Neptune (Adams et al. 2008; Rogers & Seager 2010). Super-Earths are among the most numerous planets

within the sample of detected planets, even though there are no analogs to these planets in our solar system (Mayor et al. 2011; Petigura et al. 2013; Fressin et al. 2013). Recent studies found that, within this size regime, the planet size distribution is bimodal and has a gap between 1.5 and 2.0 R_{\oplus} (Fulton et al. 2017; Fulton & Petigura 2018). The most widespread explanation for this “radius gap” is photoevaporation (Lecavelier des Etangs, A. 2007; Davis & Wheatley 2009; Ehrenreich, D. & Désert, J.-M. 2011). In this scenario, planets for which the H/He

atmosphere constitutes less than about 1% of the total mass at the time of the dispersal of the protoplanetary disk are fated to lose this atmosphere completely within about 100 Myr. In contrast, planets with initially more massive atmospheres are able to retain enough gas to cause the mean density to be substantially lower than that of a purely rocky planet. The former have completely lost their primary, hydrogen-dominated atmosphere, and therefore their (small) radius depends exclusively on the average density of the rocky core. For the latter, instead, because of the low planetary mass (i.e., low gravity) and low atmospheric mean molecular weight, the envelope extends far from the rocky surface leading to a larger planetary radius (Owen & Wu 2017; Jin & Mordasini 2018; Van Eylen et al. 2018). The planet 55 Cnc e itself is located at a very short orbital distance and exposed to more intense stellar radiation than the bulk of planets making up the populations discussed above. This planet is an example of only a handful of objects with low masses and high irradiation often referred to as ultra-short period planets (USPs).

With an orbital period of just 0.736 days, the super-Earth 55 Cnc e is an extremely hot, presumably tidally locked super-Earth with a brightness temperature of $\sim 2700 \pm 270$ K (Demory et al. 2016a). It orbits the third brightest star (V mag = 5.95; *TESS* mag = 5.48) known to host a transiting exoplanet in this size category (Winn et al. 2011; Demory et al. 2011a) after HD 39091 (Jones et al. 2002; Gandolfi et al. 2018) and HD 219134 (Motalebi et al. 2015; Vogt et al. 2015). Based on transit and radial velocity data, the radius of 55 Cnc e is $1.88 \pm 0.03 R_{\oplus}$ and the mass is $8.0 \pm 0.3 M_{\oplus}$ (Bourrier et al. 2018a). The high bulk density is $6.7 \pm 0.4 \text{ g cm}^{-3}$. Given these measurements, it is not yet possible to tell whether the planet has an Earth-like composition (an iron core surrounded by a silicate mantle) or a rocky core with an envelope of volatiles. Atmospheric escape models for such a small, highly irradiated planet predict that there should be no substantial H/He envelope (Gillon et al. 2012; Demory et al. 2016a; Kubyshkina et al. 2018) — and indeed no hydrogen exosphere has been detected (Ehrenreich et al. 2012). However, given its bulk density, the planet is most likely surrounded by a heavyweight atmosphere (Bourrier et al. 2018a).

This scenario is supported by Spitzer 4.5 μm phase curve observations (Demory et al. 2016a). These observations show an eastward offset of the hot spot of the planet and a night temperature of 1380 ± 400 K; both of these characteristics require some heat circulation. If 55 Cnc e were a “lava planet” with no atmosphere, it is unlikely that its heat redistribution efficiency would be sufficiently high to explain these two features (Kite et al. 2016; Angelo & Hu 2017). It seems more likely that 55 Cnc e has an optically thick atmosphere, as suggested by Demory et al. (2016a), Angelo & Hu (2017), and later by Bourrier et al. (2018a) through refined values of the planet mass and radius. The presence of a high-metallicity atmosphere is also indicated by the tentative detection of Ca^+ and Na in the planet exosphere (Ridden-Harper et al. 2016). The present-day atmosphere may well be shrouding a molten surface, and might have originated from volcanic outgassing.

A quasi-sinusoidal modulation in the optical flux of the 55 Cnc e system was detected using data from the Microvariability and Oscillations in Stars (MOST) space telescope (Winn et al. 2011, hereafter W11). The modulation had the same period as the planet and an amplitude initially measured at 168 ± 70 ppm. While small, this amplitude is too large to be due to only scattered light from the planet, which cannot exceed ~ 30 ppm in the MOST bandpass. For the more massive giant planet HD 20782b, similar MOST observations revealed the signature of reflected light from the planetary atmosphere as the planet passed through

Table 1. Dates, durations, exposure times, and initial number of transits (N_{tr}) corresponding to the MOST observations taken between 2011 and 2015. Note: Dates are given in Barycentric Julian Days [BJD] to within a constant 2 450 000.

Standard Year	Dates [BJD]		Duration [days]	Integration time [s]	N_{tr}
	Start	End			
2011	5599.52	5614.50	14.98	40	18
2012	5940.51	5982.67	42.16	40	52
2013	6328.78	6348.70	19.93	40	27
2014	6689.10	6713.52	24.43	60	25
2015	7033.64	7074.50	40.86	120	53

periastron (Kane et al. 2016). Therefore, W11 suggested instead that the modulation was some sort of instrumental artifact, or that it may represent a previously unknown type of star-planet interaction.

Since 55 Cnc e is not sufficiently massive to give rise to observable signatures of tidal interaction in the MOST photometry, the flux modulation at the period of 55 Cnc e may indicate the existence of magnetic interactions between the planet and its host star. A scenario involving interactions between the stellar corona activity and the planet has already been proposed by Bourrier et al. (2018b) to explain some modulation in flux observed in UV data as well. Located in a very close orbit, 55 Cnc e is an ideal target for detecting interactions that consist of an active region on the stellar surface rotating with the planet orbital motion instead of the stellar rotation period (Shkolnik et al. 2003; Walker et al. 2008; Poppenhaeger & Schmitt 2011; Lanza 2012; Strugarek et al. 2015; Shkolnik & Llama 2018; Wright & Miller 2015; Cauley et al. 2018; Strugarek et al. 2019).

Other analyses for 55 Cnc e, based on IR observations of the secondary eclipse have indicated variability in its secondary eclipse depth (Demory et al. 2016b; Tamburo et al. 2018). The authors found a 4σ difference in eclipse depth between two epochs of observations (acquired in 2012 and 2013, respectively). Demory et al. (2016b) suggested either volcanic activity or an inhomogeneous circumstellar torus of gas and dust as possible explanations. Alternatively, Tamburo et al. (2018) proposed that the planet may be intermittently covered by reflective grains originating from volcanic activity or cloud variability.

55 Cnc e has already benefited from numerous multiwavelength observations in the IR (Demory et al. 2011a, 2016b,a), UV (Bourrier et al. 2018b), and optical (W11; Gillon et al. 2012; Dragomir et al. 2014). In this paper we present an extensive dataset of optical photometry obtained with MOST, most of which has not been previously published. We use these data to provide new clues to the nature of this mysterious planet, by monitoring the time variable nature of this system, constraining the albedo of planet e and searching for transits of the other four known planets in the system. We describe the MOST observations and their reduction in Sections 2 and 3. The data analysis, results on the refined transit parameters, and discussion regarding 55 Cnc e are found in Sections 4 and 6, respectively. In Section 5 we present a search for transits of the other known planets in the system, and we conclude in Section 7.

2. MOST observations of 55 Cnc

The MOST telescope (Walker et al. 2003; Matthews 2004) is a now inactive microsatellite carrying a 15 cm optical telescope,

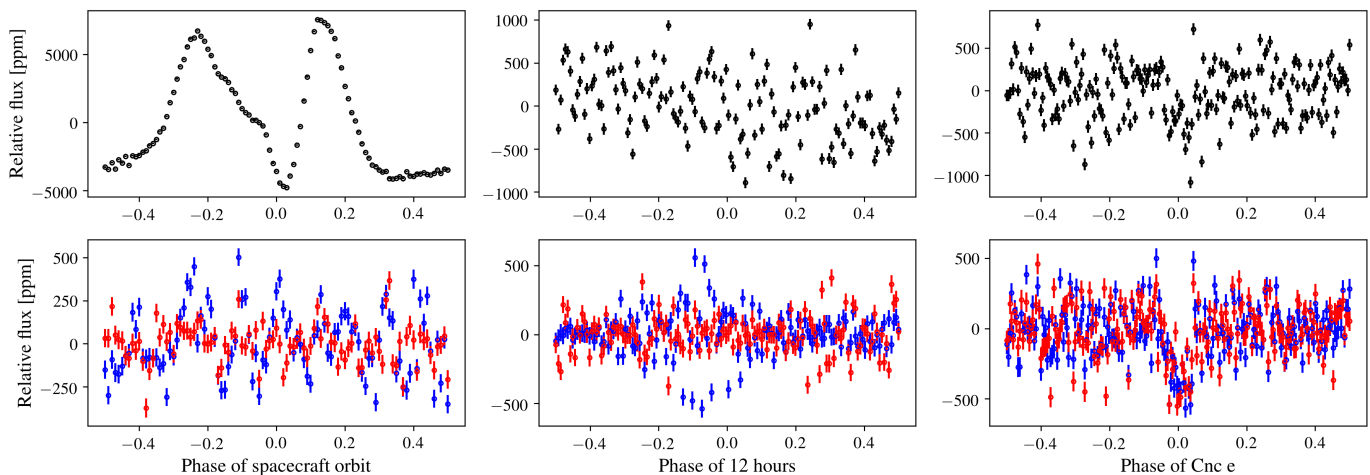


Fig. 1. MOST data obtained in 2015 after pre-whitening (top panels, see Sec. 3.1) and after the correction of the Earth stray-light variations (bottom panels, see Sec. 3.2). We show the relative flux phase folded at the satellite period (left, binned into 1-minute), a period of 12 hours (middle, binned into 5 min), and the planet period (right, binned into 5 min). In the bottom panels, observations detrended by the classical procedure (see Sec. 3.2.1) are shown in blue and by the time-shift procedure (see Sec. 3.2.2) in red. In these plots, the uncertainties are based on the original unscaled photometric uncertainties.

which acquires light through a broadband filter spanning the visible wavelengths from 350 to 700 nm. This instrument remains in a Sun-synchronous polar orbit with a period of 101.4 minutes, which allowed it to monitor stars in a continuous viewing zone (CVZ) without interruption for up to eight weeks. The CVZ covered a declination range from $+36^\circ > \delta > -18^\circ$. Stars brighter than $V \sim 5 - 6$ were observed using a Fabry microlens to project onto the CCD an image of the telescope pupil illuminated by the target. Fainter stars were observed in direct imaging mode, in which the defocused images of the stars were projected onto the CCD (Rowe et al. 2006).

55 Cnc was in the CVZ of MOST, and was observed every year from 2011 to 2015 with timespans between about 15 and 42 days. The observations were acquired in direct imaging mode with an exposure time of 0.5 s per individual frame. The images were downloaded from the satellite in stacks of 40 to 240, resulting in total integration times ranging from 20 to 120 s (excluding overheads) per downloaded data point. Including overheads, the sampling rate ranged from 20.91 to 124.44 s. Table 1 shows the dates, duration, and exposure times used for each of the five time series.

Raw light curves were extracted from the images using aperture photometry. We found that an aperture radius of five pixels almost always gave the lowest scatter in the residuals, so for consistency we used this size to extract all of the MOST photometry. We detail the reduction and analysis of the light curves in the next section.

3. Photometric analysis

There are several challenges in reducing MOST observations to obtain the final light curves (Rowe et al. 2006). In the steps detailed below, we independently reduce each of the five datasets taken between 2011 and 2015. We note that the first two datasets (2011-2012) have already been presented in W11 and Dragomir et al. 2014; hereafter D14). The detrending steps used in the present study follow established methods used to reduce MOST datasets (Rowe et al. 2006, W11, D14).

3.1. Data pre-whitening

The first step consists in removing the extreme outliers exceeding ten standard deviations (σ) from the median flux. To obtain a homogeneous time series for each dataset, and also because we observed correlations between the significant outliers and different integration times, we removed data points with integration times differing from the values given in Table 1.

For each year, we fit the entire dataset (15 to 42 days) with a fifth degree polynomial function of both the sky background and pixel-to-pixel shifts. We then divided the time series by the best-fit polynomials to obtain a corrected, normalized sequence. Then, we again eliminated outliers lying above 5σ from the median flux ($< 0.5\%$ of the time series).

After these steps, we removed some parts of the light curves that are affected by large observational gaps (mainly due to tracking lost). We find that doing so increases the signal-to-noise ratio (S/N) of the detected transits. Indeed, observations surrounding these data gaps show a particularly large number of outliers compared to the remaining values. For the 2011 dataset, we removed the first 0.6 and last 2.1 days (as done in W11), for 2012 we removed the first 0.5 and last 5.85 days, for 2013 only the last 2.67 days, for 2014 the first 8.31 and last 0.643 days, and for 2015 the first 10.71 days (see Appendix. A).

In the resulting sequences, we observed a long-term variation that may be due to stellar activity; the stellar rotation period is 38.8 days (Bourrier et al. 2018a). This variation is shown and discussed in Appendix. A. This had to be corrected before we could make the final correction of patterns related to the satellite motion (see Sec. 3.2). We proceeded as follows: we first masked transits and secondary eclipse, and then binned the observations into intervals of twice the planet orbital period. Then, we fit a spline function to the binned data, and removed it from the initial unbinned sequence. We have investigated several alternatives to this technique (e.g., boxcar, Gaussian or Savitzky & Golay 1964 filters) but, as long as we consider filter sizes larger than twice the planetary period, all of these approaches lead to similar results.

3.2. Correction for stray-light variations

The MOST satellite completed one polar orbit around Earth in $P_{sat} = 101.4$ min. Its observations are affected by the scattered Earthshine, which generates flux variations with amplitudes that vary from orbit to orbit depending on the part of the Earth visible to the satellite. These variations are modulated with both the orbital period of the satellite and the Earth's rotation period. An example of a pattern observed at P_{sat} is shown in the top left panel of Fig. 1, while the sinusoidal-like pattern observed at the Earth's rotation period is shown in the top middle panel. As discussed in W11, the stray-light timescales and amplitudes are too different from the orbital period of planet e to mimic the variations observed at the planetary period (see Sec. 4.2). However, the orbital period of the satellite is comparable to the planet transit duration (≈ 95 min) and the correction of the stray-light patterns should be done carefully to avoid any influence on the inferred transit parameters.

3.2.1. Classical method

The shape of the variations induced by stray-light is variable from one satellite orbit to another. In panel (a) of Fig. 2, we show the one-day sequences of the 2012 dataset phase folded on the satellite orbital period. Each of these shorter sequences contains approximately $14 P_{sat}$. We observe a variability in the shape of the pattern and a time delay between the distinct features. These variations illustrate a need to treat MOST observations on a similar timescale. Traditional techniques (Rucinski et al. 2004; Rowe et al. 2008; Dragomir et al. 2013) consist in correcting these stray-light systematics on short sequences (e.g., of two-day length). Typically, the short time series are phase folded at the satellite orbital period and a moving average filter is iteratively removed for each of them. In this paper, we performed a similar technique to correct for the stray-light variations, which is detailed below:

1. Select a one-day time-series (corresponding to $\sim 14 P_{sat}$)
2. Mask transits and eclipses
3. Phase fold on satellite orbital period
4. Use a Savitzky-Golay (SG) filter of window size w_1 (instead of a moving average) to model the detailed variability at the MOST period
5. Remove this variability from the entire one-day sequence (including transits and eclipses)
6. Unfold the subseries
7. Repeat steps 1 to 6 for each one-day sequence

Then, as some correlated noise remains, we removed the final structures related to the orbital period of the satellite and the Earth's rotation period as follows:

8. Mask transits and occultations from the entire light curve
9. Phase fold the series at the MOST orbital period
10. Use a SG filter (of width w_2) to model the residual variability at the satellite period
11. Remove this variability from the entire light curve (including transits and eclipses)
12. Repeat steps 8 to 11 for the satellite period harmonic $P_{sat}/2$ (using width w_2), the Earth's rotation period and its 12-hour harmonic (using width w_3)
13. Unfold the series and remove the final 3σ outliers from the median value

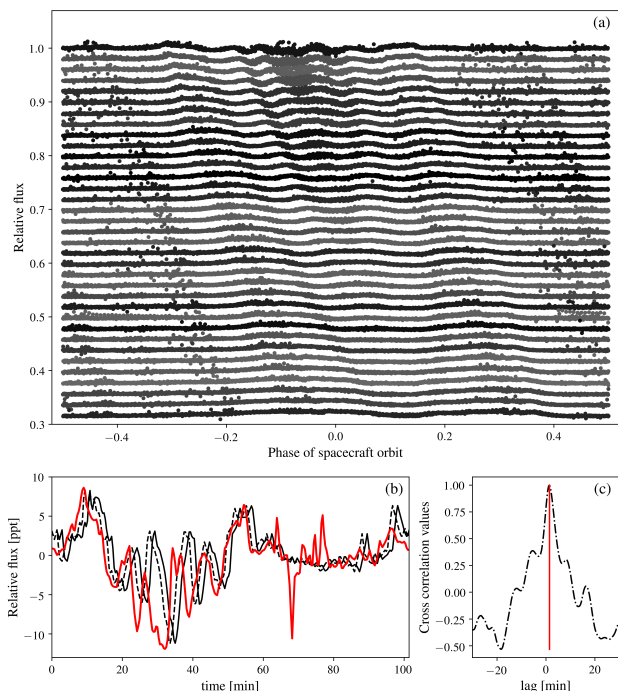


Fig. 2. Illustration of the Earth stray-light variation with respect to the orbital period of the satellite (2012 dataset). (a) Relative flux of the one-day sequences phase folded at the MOST satellite period and binned over 5-min intervals. The different series have been shifted in flux for visibility. The shape of the stray-light evolves from day-to-day and a time delay is observed. (b) Example of patterns with a duration of one satellite period belonging to the same one-day time series. The y-axis is in part-per-thousand. The solid lines show an unshifted (black) and the reference (red) pattern. The dashed line shows the black pattern corrected by the estimated time delay (-86s), which was found using the cross-correlation function shown in (c).

We chose the different parameters involved in this procedure (length of the subseries, window sizes of the filters, and sigma clipping level) such that they maximize the final S/N of the known planetary transits (evaluated using Equation (2) of Pont et al. 2006). Table 2 lists the best window widths $\{w_1, w_2, w_3\}$ found during this procedure, the final root-mean-square (rms) measured out-of-transit and the transit S/N for the different sequences (first horizontal box). The final length of the observations (T_{obs}), the number of data points (N_{pts}), and the number of transit events (N_{tr}) are also indicated at the end of the table. When the datasets are combined, we count 157 770 data points and 143 transit events.

The bottom panels of Fig. 1 show this light curve detrending procedure (blue lines), illustrating how stray-light variations related to P_{sat} (left) and the Earth rotation (middle) are removed. Fig. 3 shows the combined light curve phase folded at the planetary orbital period and Fig. 4 shows each sequence between 2011 and 2015 (left column).

The detrended light curve corresponding to the 2011 dataset (top left panel of Fig. 4) is comparable with that reduced by W11 using a similar detrending technique based on moving average filters. However, we obtain a slightly higher scatter than W11 at the transit location owing to the transit masking steps added to the procedure described above (steps 3 and 8).

Table 2. Parameters involved in the classical and time-shift detrending procedures. Note: † SG window widths have to be uneven, the rms units are ppm, and T_{obs} is in days.

	Year	2011	2012	2013	2014	2015
Classic	w_1 †	27	7	7	27	7
	w_2 †	331	681	837	341	801
	w_3 †	357	751	957	217	57
	rms	1016	1031	722	915	1213
	S/N	13.9	26.7	20.9	15.9	10.2
Time-shift	w_1 †	27	39	91	43	27
	w_2 †	261	861	131	321	711
	w_3 †	2111	121	2031	671	171
	rms	995	1084	773	561	1162
	S/N	13.9	26.8	21.2	16.4	9.4
N_{pts}	21 236	67 445	32 521	17 811	18 757	
T_{obs}	12	35	17	14	29	
N_{tr}	16	47	23	18	39	

3.2.2. Improvement of the traditional detrending method: Time-shift procedure

We propose an alternative method to improve the modeling of the stray-light pattern modulated at the satellite orbital period (step 4 of the classical procedure). As shown in panel (a) of Fig. 2, we observe a variability in both the shape of the pattern and a time delay between the distinct features.

However, smaller time delays are also present between individual orbits during the one-day sequences shown in Fig. 2. To take these into account, we developed a new technique that consists in cross-correlating each of the 14 individual P_{sat} features with a reference sequence; because of small data gaps we used the sequence with the largest number of data points. During this step, both transits and eclipses are masked. After compensating the time delay for each of the sequences, we isolated the general pattern using a SG filter (width w_1) and removed it from the considered one-day time series (containing transits and eclipses). Then, we applied steps 5) to 12) of the classical procedure described above. An example of the time delay between two consecutive patterns is shown by the black and red solid lines in panel (b) of Fig. 2. A normalized cross-correlation function derived from two of these short series is shown in panel (c), where we find a time shift of -86 seconds. The dashed black curve in panel (b) shows the black feature shifted by this delay to match the reference feature.

The middle box in Table 2 lists the parameters involved in this new procedure as well as its performance in terms of rms and transit S/N. While the increase (resp. decrease) of the transit S/N (resp. rms) is not drastic, the benefit of this procedure can be seen in the comparison of the final light curves. The 2015 light curve phase folded at the spacecraft orbital period resulting from this time-shift procedure is shown in red in the bottom right panel of Fig. 1. We see that, even if it does not increase the transit S/N (see last column of Table 2), the time-shift method significantly reduces the systematics induced by stray-light occurring at the timescale of the spacecraft orbit. The light curves phase folded at the planet orbital period are shown in the middle panel of Fig. 4. Comparing these light curves with those obtained from the classical procedure (Fig. 4, left column), we see a reduction of the remaining pattern modulated with the orbital period of the satellite ($\sim 1/10$ of the planet period). This effect is particularly remarkable for the 2011 dataset (top panels). However, as we see in Sec. 4, this correction does not significantly affect the

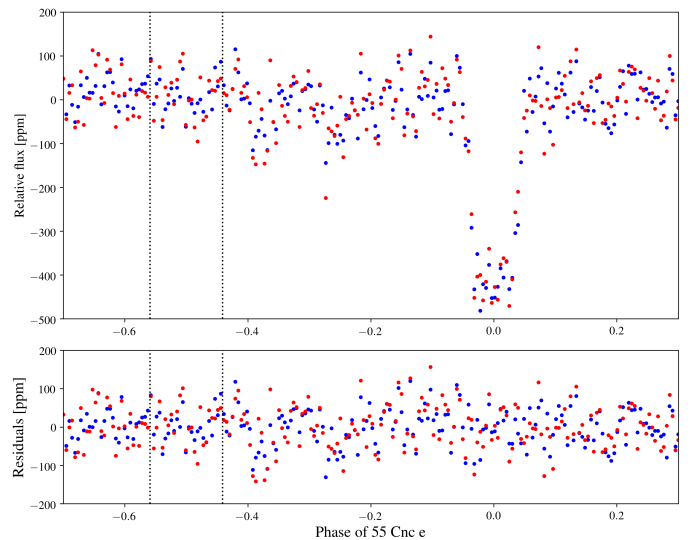


Fig. 3. Combine light curve phase folded at the planet orbital period and binned into 5-min intervals (top) and associated residuals (bottom). The observed phase modulation has been removed using results given in Sec. 4.2 to compare only the transit shape. Observations detrended by the classical procedure are shown in blue and by the time-shift procedure in red. At the timescale of the planet orbital period, the light curves are globally identical (S/N ~ 40 , rms ~ 1000 ppm). The phase range of the secondary eclipse are indicated by the vertical dotted lines.

features occurring at the timescale of the planet orbital period ($> 10P_{sat}$). At this timescale, the light curves detrended by both procedures remain comparable with a similar transit S/N when the light curves are combined (S/N of 40.2, see Fig. 3). A better visualization of the detected modulation in flux is shown in Fig. 5 for the light curves detrended by the time-shift procedure with the transit model removed.

We finally note that the time-shift method could also be applied on the whole time series to correct the time delay between all orbits globally. However, as the shape of the stray-light pattern changes significantly over the course of several days, this would degrade the accuracy of the correction.

4. Transit properties of 55 Cnc e

To interpret our data, we performed a Markov Chain Monte Carlo (MCMC) analysis using both the light curves detrended via the classical method, with and without the time-shift correction. A detailed description of the MCMC scheme can be found in Lendl et al. (2017). We used the Mandel & Agol (2002) algorithm to model transits and occultations, and the differential-evolution MCMC engine described in Cubillos et al. (2017). As our datasets do not have a high enough S/N to fit for stellar limb darkening, we used a quadratic limb-darkening law with fixed parameters that have been derived for the MOST bandpass: $u_1 = 0.648$ and $u_2 = 0.117$ (D14). To derive the transit, phase variation and secondary eclipse parameters, we carried out our analysis in three steps.

First, we fit for the transit period (P), epoch of mid-transit (T_0), planet-to-star radius ratio (R_p/R_s), impact parameter (b), and transit duration (t_d) to estimate precisely the planetary orbital period. Second, we fixed the orbital period and proceeded to a second fit of the light curve, combining the transit model with a function modeling the variations in flux observed at the planetary period (see Fig. 4). We added these variations to the

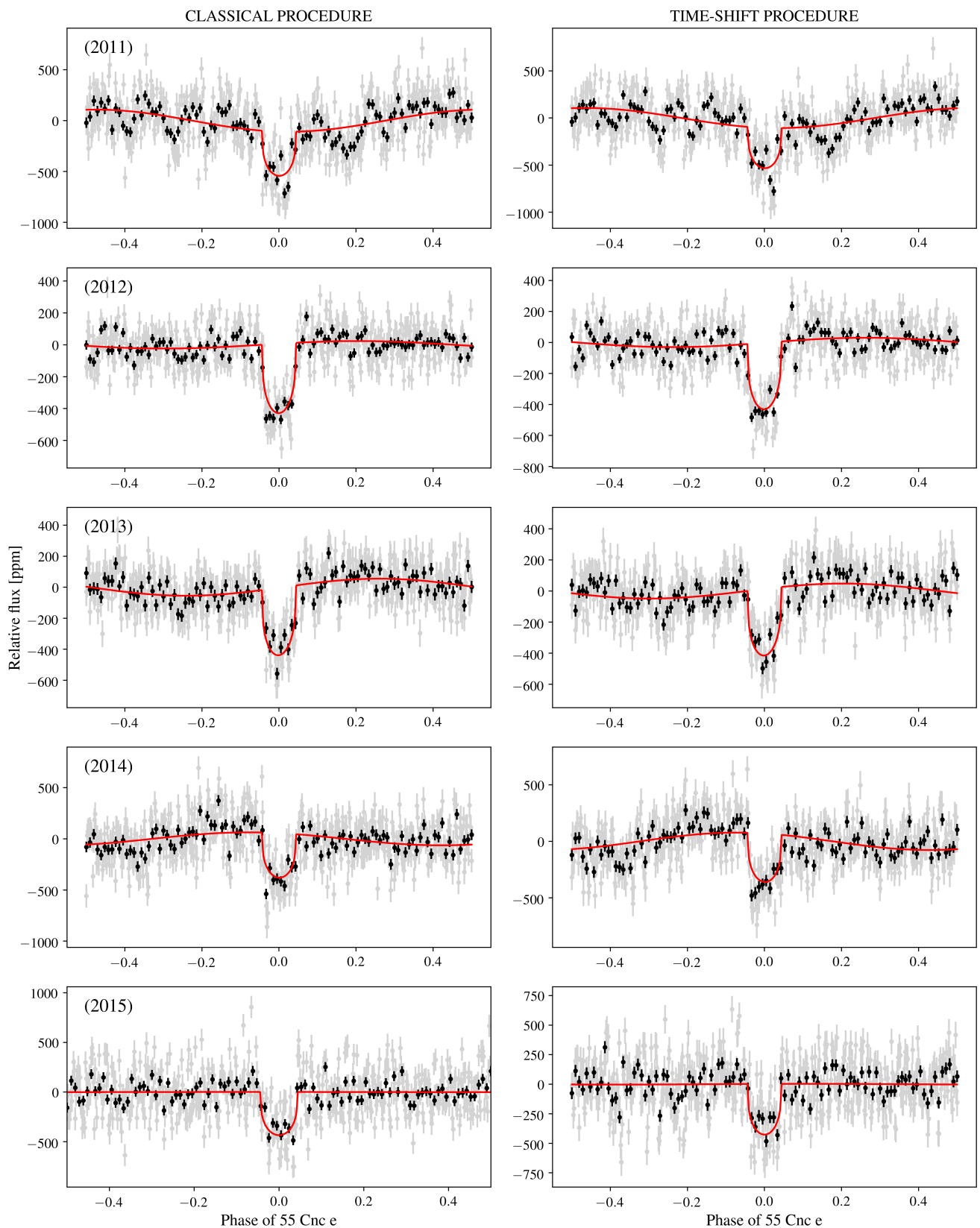


Fig. 4. Light curves phase folded at the planet orbital period and binned into 2 (gray) and 10-min (black) intervals. From top to bottom, we show data taken in 2011, 2012, 2013, 2014, and 2015. The first column shows the final light curves obtained via the classical detrending procedure and the second column shows the light curves obtained via the time-shift detrending procedure. In these plots, the uncertainties are based on the original unscaled photometric uncertainties (in contrast to the scaled errors used in the MCMC analyses, see Sec. 4.4). The best-fitting models are shown in red.

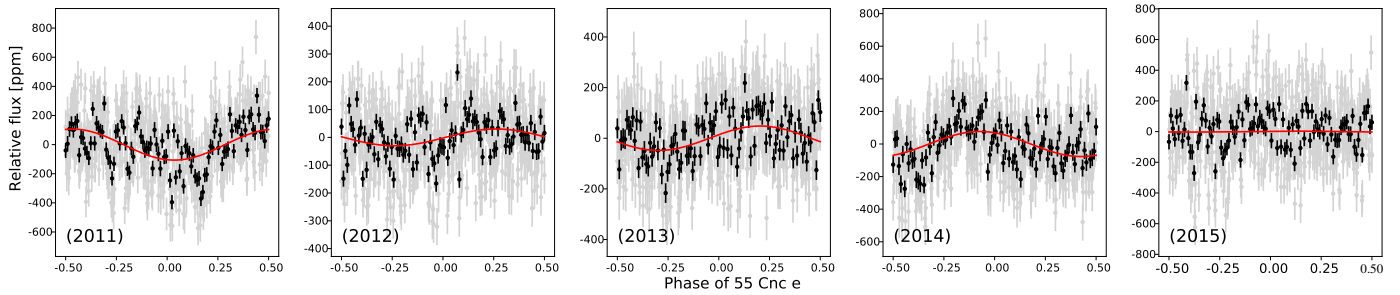


Fig. 5. Light curves detrended by the time-shift procedure, without transits, phase folded at the planet orbital period and binned into 2 (gray) and 10-min (black) intervals.

transit model as sinusoidal functions of (fixed) planetary orbital frequency $f_s = 1/P$:

$$F_{\text{mod}}(t) = \alpha_{\text{mod}} \sin(2\pi f_s t + \phi_{\text{mod}}), \quad (1)$$

where the vectors α_{mod} and ϕ_{mod} collect all the information about the amplitudes and orbital phases (relative to mid-transit) of the various datasets (simplified hereafter as $\{\alpha_i, \phi_i\}$ with $i \in [2011, 2012, 2013, 2014, 2015]$). In this analysis, we simultaneously estimated 14 free parameters (4 for the transit and 5×2 for the phase variation). Finally, we removed the best-fitting models of transit and phase modulation from the time series and fit the secondary eclipse depth.

Following the reassessed transit parameters of [Bourrier et al. \(2018a\)](#), we assumed an eccentricity of zero for the orbit of the planet and added a prior on the impact parameter ($b = 0.39 \pm 0.03$) to help convergence. The results are described below and the best-fitting models for transit and phase modulation for each year are compared in Fig. 6.

4.1. Updated 55 Cnc e parameters

With 143 transit events, we precisely estimated the planetary orbital period of 55 Cnc e. This value, found during the first MCMC analysis, is given in the first row of Table 3. Results found on the time series detrended by the classical and time-shift methods are in complete 1σ agreement with each other as well as with the period extracted through velocity measurements ([Bourrier et al. 2018a](#)). When estimating the flux modulation parameters, the orbital period has to be fixed to ensure the convergence of the second MCMC. The inferred transit and phase modulation parameters obtained during this second fit are given in Tables 3 and 4, respectively. The associated marginal posteriors are reported in Fig. 13 and the best-fitting models are shown in Fig. 6. Once more, we find similar parameters from light curves detrended via the classical and via the time-shift methods. Moreover, the parameters derived from the first and second MCMC agree to better than 1σ . The most significant difference is for the transit depth that slightly decreases (< 5 ppm) between the two runs because of the addition of the phase modulation in the second fit. All values for the transit parameters are in 1σ agreement with the values published by [Bourrier et al. \(2018a\)](#) and the previous results based on MOST data by W11 and D14. However, we note that we find slightly shallower transits (at approx. 1σ) than W11 and D14.

4.2. Phase variations

Contrary to previous analyses of MOST data (W11, D14), our phase curve model (see Eq. (1)) allows the flux maximum to be

offset in time from the planetary occultation. Furthermore, we fit independent phase curve parameters for each year, thus probing temporal variability. Fig. 7 illustrates the evolution of the phase modulation from year to year. The phase variation, initially observed in the 2011 dataset by W11, is seen during most of the subsequent years, but its phase and amplitude change. In 2011, the phase variation amplitude is the highest. In 2012, it seems to be attenuated in comparison to the 2011 dataset. In 2013 and 2014, it is present, although with a different phase and amplitude. We find no modulation in 2015, however this dataset is the noisiest and the phase variation might be masked by residual correlated noise (see rms values given in Table 2). Compared to W11, the derived amplitude of the phase modulation measured in the 2011 dataset is smaller¹ but agrees within 1σ . When analyzing the light curves of 2011 and 2012 together, and fitting for a common phase modulation for both years, we find an amplitude of $\alpha_{2011+2012} = 24_{-7.8}^{+8.7}$ ppm that agrees with the results² of D14. However, as the modulation changes significantly with time (see Fig. 7), we argue that combining light curves from several years tends to attenuate the observed modulation.

We note that we attempted to probe shorter timescales of the phase curve variability by studying subsets of our five MOST datasets, but the quality of the data at hand are not sufficient to draw meaningful conclusions; i.e., the signal at the planet period only significantly appears when a sufficiently large number of planet periods are phase folded.

4.3. Secondary eclipse

To search for the secondary eclipse of 55 Cnc e, we first divided the data by our best-fitting transit and flux modulation models. Then, we performed a final MCMC analysis of the light curve residuals of all observations. Previous analyses from D14 did not detect the secondary eclipse, and these authors estimated the depth of this eclipse to be -1_{-22}^{+18} ppm (using the MOST data of 2011 and 2012). Expecting an extremely shallow signature of the planetary eclipse and to ensure obtaining a representative posterior distribution, we allowed the depth parameter to take negative values in our MCMC analysis (no physical meaning).

We find an eclipse depth of $\delta_{\text{ecl}} = -12.88_{-7.6}^{+8.9}$ ppm. Consequently, we do not detect any optical signature of the secondary eclipse of 55 Cnc e, but we can place a 2σ limit of 16 ppm on its depth using the posterior distribution. Fig. 3 shows the multiyear light curve phase folded on the period of 55 Cnc e, where the phase range of the secondary eclipse is indicated by dotted lines.

¹ Winn et al. found $\alpha_{2011} = 168 \pm 70$ ppm.

² Dragomir et al. found $\alpha_{2011+2012} = 34_{-11}^{+12}$ ppm.

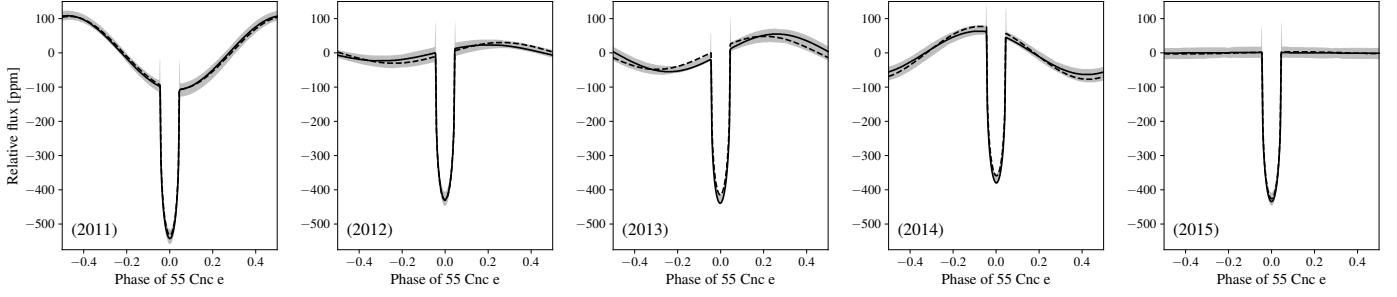


Fig. 6. Best-fitting models resulting from the MCMC analysis as described in Sec. 4, using the light curves detrended by the classical (solid) and time-shift (dashed) procedures. For the latter only, we display the 1σ uncertainties (gray shaded area). These uncertainties have been evaluated using 10^4 transit models generated using transit and phase modulation parameters randomly taken from the MCMC posteriors.

Table 3. Inferred transit parameters for 55 Cnc e obtained using the light curves detrended by the classical (CM) and time-shift (TM) procedures and their 1σ uncertainties. The last column indicates the most recent values published in Bourrier et al. (2018a). Notes: All the 1σ uncertainties were derived using the distribution of the parameter posteriors. The impact parameter was completely determined by the input prior.

	Parameter	Symbol	Units	Value (CM)	Value (TM)	Bourrier et al.
Measured parameters	Orbital period	P	days	$0.73654530^{+6.5\times 10^{-7}}_{-9.5\times 10^{-7}}$	$0.73654504^{+7.6\times 10^{-7}}_{-9\times 10^{-7}}$	$0.73654737^{+1.3\times 10^{-6}}_{-1.44\times 10^{-6}}$
	Transit epoch	$T_0 - 2\,451\,545$	BJD	$4417.0720^{+6.1\times 10^{-4}}_{-3.6\times 10^{-4}}$	$4417.0719^{+6.6\times 10^{-4}}_{-5.0\times 10^{-4}}$	$4417.0712^{+1.4\times 10^{-3}}_{-1.4\times 10^{-3}}$
	Planet-to-star radius ratio	R_p/R_s		$0.01874^{+3.9\times 10^{-4}}_{-2.9\times 10^{-4}}$	$0.01860^{+3.2\times 10^{-4}}_{-4.0\times 10^{-4}}$	$0.0182^{+2\times 10^{-4}}_{-2\times 10^{-4}}$
	Impact parameter	b		$0.3917^{+0.029}_{-0.033}$	$0.3954^{+0.027}_{-0.035}$	$0.39^{+0.03}_{-0.03}$
	Transit duration	t_d	days	$0.0648^{+1.1\times 10^{-3}}_{-0.9\times 10^{-3}}$	$0.0654^{+0.9\times 10^{-3}}_{-1.4\times 10^{-3}}$	$0.0634^{+3.7\times 10^{-4}}_{-3.7\times 10^{-4}}$
	Eclipse depth	δ_{ecl}	ppm	$-9.99^{+7.5}_{-10.6}$	$-12.88^{+8.9}_{-7.6}$	
Derived parameters	Transit depth	$(R_p/R_s)^2$	ppm	$351.33^{+11.16}_{-14.68}$	$346.11^{+11.99}_{-14.90}$	$331.24^{+7.28}_{-7.28}$
	Planetary radius	R_p	R_\oplus	$1.8865^{+0.045}_{-0.035}$	$1.90^{+0.037}_{-0.047}$	$1.875^{+0.029}_{-0.029}$
	Scaled semimajor axis	a/R_s		$3.4746^{+6.9\times 10^{-2}}_{-7.2\times 10^{-2}}$	$3.5046^{+6.4\times 10^{-2}}_{-9.4\times 10^{-2}}$	$3.52^{+1.0\times 10^{-2}}_{-1.0\times 10^{-2}}$
	Semimajor axis	a	AU	$0.01521^{+3.7\times 10^{-4}}_{-3.4\times 10^{-4}}$	$0.01528^{+4.1\times 10^{-4}}_{-3.5\times 10^{-4}}$	$0.01544^{+5.0\times 10^{-5}}_{-5.0\times 10^{-5}}$
	Orbital inclination	i	deg	$83.56^{+0.61}_{-0.62}$	$83.72^{+0.49}_{-0.74}$	$83.59^{+0.47}_{-0.44}$

We estimated the upper limit on the geometric albedo (A_g) of 55 Cnc e using the following equation (Rowe et al. 2008):

$$\delta_{ecl} = A_g \left(\frac{R_p}{a} \right)^2. \quad (2)$$

Given the very close orbit of 55 Cnc e, we compared its predicted thermal contribution with our upper limit on the eclipse depth using our R_p/R_s value, a stellar effective temperature of 5172 ± 18 K (Yee et al. 2017), and two values for the planet temperature: 2300 K, which is the highest value of the predicted equilibrium temperature (with zero albedo and zero heat redistribution; Crossfield 2012); and 2700 K, which is the hemisphere-averaged value measured by Demory et al. (2016a). The thermal contribution is 0.9 and 4 ppm, for each of those two cases, respectively. In this section we derived 2σ albedo limits for both

cases, but we used and referred to the value corresponding to the measured temperature (2700 K) throughout the remaining sections of this paper.

We first subtracted the thermal contribution from the 2σ limit on δ_{ecl} , and used the resulting value in equation 2. We then derived a 2σ lower limit on R_p/a from the corresponding lower limit on R_p/R_s from the second-to-last column of Table 3, and from the corresponding upper limit on a/R_s from Bourrier et al. (2018a, as their value is in agreement with and more precise than ours). We thus obtained 2σ upper limits on A_g of 0.59 and 0.47, assuming planet temperatures of 2300 and 2700 K, respectively.

Table 4. Inferred parameters of the modulation in flux observed at the planet orbital period. Results obtained using the light curves detrended by the classical and time-shift procedures are shown at left and right, respectively.

Classic			Time-shift		
Year	Amplitude (α_{mod})	Phase (ϕ_{mod})	Year	Amplitude (α_{mod})	Phase (ϕ_{mod})
2011	$108.54^{+12.8}_{-16.6}$ ppm	$0.19^{+0.27}_{-0.19}$ rad	2011	$106.52^{+12.5}_{-18.4}$ ppm	$0.13^{+0.26}_{-0.13}$ rad
2012	$23.49^{+8.2}_{-9.7}$ ppm	$2.20^{+0.33}_{-0.47}$ rad	2012	$30.19^{+8.3}_{-9.5}$ ppm	$1.84^{+0.36}_{-0.24}$ rad
2013	$54.96^{+15.6}_{-11.2}$ ppm	$1.85^{+0.27}_{-0.19}$ rad	2013	$48.3^{+12.1}_{-14.2}$ ppm	$2.21^{+0.26}_{-0.29}$ rad
2014	$63.43^{+14.1}_{-14.9}$ ppm	$3.98^{+0.21}_{-0.26}$ rad	2014	$77.01^{+15.1}_{-15.3}$ ppm	$3.94^{+0.20}_{-0.18}$ rad
2015	$-0.77^{+14.3}_{-14.7}$ ppm	$0.70^{+0.65}_{-0.62}$ rad	2015	$-3.05^{+17.3}_{-13.4}$ ppm	$0.94^{+0.28}_{-0.30}$ rad

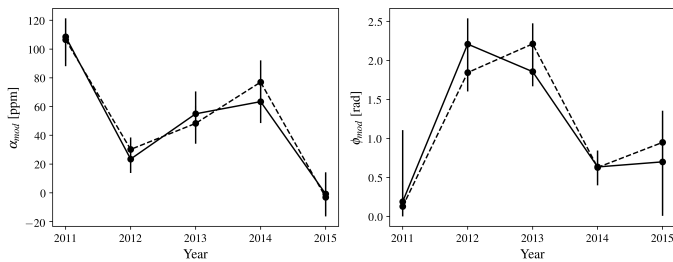


Fig. 7. Evolution of the amplitudes (left) and orbital phases (right) parameters of the modulation in flux observed at the planet orbital period (see Eq. 1). The solid and dashed lines indicate the light curves detrended by the classical and time-shift procedures, respectively.

4.4. Uncertainties of the inferred parameters

To validate the uncertainties on both the phase modulation parameters and the eclipse depth, we performed injection tests as done in W11. These tests consist in injecting a synthetic signal (either the secondary eclipse or the phase modulation) in the light curve residuals and performing an MCMC analysis of these synthetic light curves to estimate the parameters of interest. For both cases, we used the 2013 data only to save on computation time and performed 1000 individual injections. We used an eclipse depth of $\delta_{\text{ecl}} = 5$ ppm and a phase modulation amplitude of $\alpha_{13} = 45.63$ ppm. When injecting secondary eclipses, the time at mid-eclipse is randomly chosen between $[t_0 - t_d/2, t_0 + P - t_d/2]$. When injecting a phase modulation, the phase parameter Φ_{13} is randomly chosen between $[-2\pi, 2\pi]$.

Fig. 8 shows the distribution of the best-fitting values for the recovered eclipse depth (top) and the parameters α_{13} and Φ_{13} (bottom). For the secondary eclipse depth, we find a bimodal distribution around the true injected value (green dashed line). This distribution is centered around the true value, but is clearly not Gaussian. This illustrates the influence of the correlated noise still present in the reduced light curves. Depending on the injected secondary eclipse timing, its depth is over — or under — estimated as a consequence of the average level of correlated noise at this orbital phase. From these tests, we estimate a realistic uncertainty on the occultation depth of up to 35 ppm (measured as the maximum dispersion around the true value of 5 ppm).

For the phase modulation, the distribution of the retrieved values for amplitude and phase are centered around the true values. The widths of the two distributions are 7 ppm and 0.2 rad for amplitude and phase, respectively. These results show that

the impact of the remaining correlated noise is less significant on timescales longer than the satellite orbital period; i.e., they do not affect the modulation in flux related to the planet orbit, for which we also have many more photons.

Beside the injection tests, we also tested whether reliable uncertainties can be obtained by scaling the input errors. The MCMC code used in this work uses the χ^2 as its merit function, however this implicitly assumes white Gaussian noise. As correlated noise persists in the data even after the corrections described in Section 3.1, this would lead to largely underestimated errors on the derived parameters. Therefore, we scale our photometric errors. We use the β_r factor that compares the ratio of standard deviations evaluated on the binned and raw residuals (Winn et al. 2008; Gillon et al. 2010). We tested bin intervals between 5 and 20 minutes and scaled the error bars by the highest value found. We find that a relatively large factor of $\beta_r = 2.262$ allows us to obtain similar uncertainties on the phase curve parameters as those derived using injection tests.

The uncertainties given in Tables 3 and 4 were derived using this β_r method. We note that for the secondary eclipse search, we used the errors scaled during the second MCMC analysis.

5. Search for transits of 55 Cnc b, c, f, and d

There are four other known planets in the 55 Cnc system that have been detected via radial velocity measurements (Fischer et al. 2008; Dawson & Fabrycky 2010). Given that the innermost one, i.e., planet e, transits the host star, there is a non-negligible probability that one or more of the others may transit as well. Their masses and orbital periods span wide ranges (Dawson & Fabrycky 2010), forming an extrasolar multiple planet system that is moderately similar to our solar system. 55 Cnc f holds particular interest because it spends about 74% of its eccentric orbit within the habitable zone of the system (von Braun et al. 2011); we note that this statement may no longer be true as the recent re-evaluation of the eccentricity is now consistent with zero (Bourrier et al. 2018a).

Using parameters given in Table 3 of Bourrier et al. (2018a), we computed the predicted transit times during our MOST observations for the five innermost planets. Fig. 9 shows the MOST data phase folded at the orbital period of the planets with the 1, 2, and 3σ uncertainties of their time at mid-transit. When using the MCMC routines described above to search for transits of each of these planets, we come up empty. However, assuming the innermost planets b and c were transiting, we can give an upper limits on their planetary radii. Considering $b = 0.5$ as the

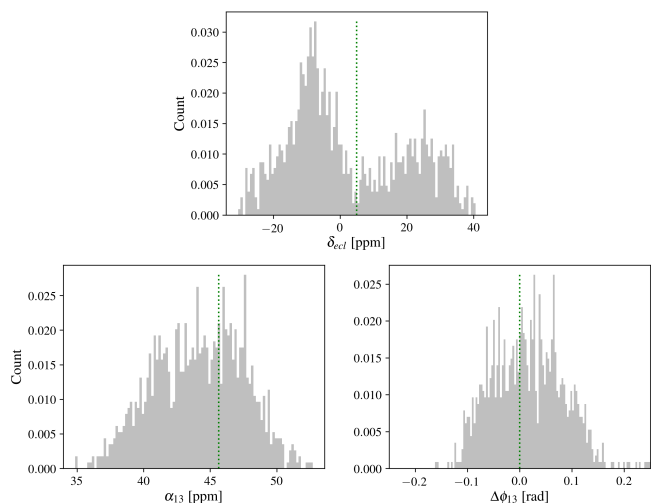


Fig. 8. Normalized distribution of the best-fitting values obtained from injection tests performed for the planetary eclipse (top) and for the phase modulation (bottom). The synthetic eclipse depth has been set to 5 ppm and the phase modulation amplitude to $\alpha_{13} = 48.3$ ppm. In the bottom right panel, we show the difference between the inputs and estimates of the phase parameter ($\Delta\Phi_{13}$) as the input phase value is randomly changing from one test to another.

nominal value (because the orbital inclination of each of these planets' orbit is unknown), we predict an upper limit of $2.15 R_{\oplus}$ for planet 55 Cnc b and $2.56 R_{\oplus}$ for planet 55 Cnc c (assuming a limiting S/N of 40 as planet e).

6. Discussion

6.1. Albedo of 55 Cnc e

While we do not detect a secondary eclipse of 55 Cnc e, we can consider the 0.47 upper limit on its albedo in the context of other albedo measurements in the literature. Thanks to *Kepler* and *K2*, it has been determined that hot Jupiters are typically dark and likely cloudless (i.e., $A_g < 0.2$; Esteves et al. 2015; Angerhausen et al. 2015). A few hot Jupiters have A_g values between 0.2 and 0.35 (Esteves et al. 2015; Angerhausen et al. 2015; Demory et al. 2011b), indicating that a small fraction of these planets have clouds.

However, 55 Cnc e should be compared to planets of its own size. Albedo measurements of the Kepler close-in super-Earth and Neptune sample as a whole have revealed that these worlds are somewhat less dark than hot Jupiters, but still have A_g values generally below 0.3 (Demory 2014; Sheets & Deming 2017; Jansen & Kipping 2018). One exception is the hot rocky exoplanet Kepler-10b (Batalha et al. 2011). Rouan et al. (2011) suggested ThO_2 particles dispersed in Al_2O_3 -CaO lava as a possible origin for the relatively high (0.32) geometric albedo of the planet.

If the surface of 55 Cnc e is molten (Demory et al. 2016a) and assuming that at visible wavelengths we can view all the way to its surface, Kane et al. (2011) predicted a secondary eclipse depth of 20 ppm using an A_g value of 0.6. However, recent preliminary laboratory measurements of specular reflection from molten lava and quenched glass (a product of rapidly cooled lava) suggest an upper limit on the albedo of such a planetary surface of 0.1 (Zahra Essack, MIT, private communication). While we note that the albedo of molten rock depends on the composition of the mantle of the planet, which is unknown for

55 Cnc e, a molten surface unobstructed by an atmosphere (at the wavelengths probed by the MOST data) remains possible within our A_g upper limit.

While our constraints on the geometric albedo of 55 Cnc e do not rule out any of the most likely atmospheric composition models (e.g., CO, CO_2 , H_2O , N_2 , O_2 , HCN; Angelo & Hu 2017; Miguel 2019), we can provide a first test of the model proposed by Tamburo et al. (2018) to explain the previously observed IR secondary eclipse variability (Demory et al. 2016b). Tamburo et al. (2018) found that refractory particulates produced by volcanic activity, at times lofted high in the atmosphere, could obscure the surface of the planet and potentially explain the decrease in observed thermal emission. According to this model, 55 Cnc e would have a higher albedo (between 0.4 and 1.0) when its surface is obscured by the refractory particulates. In this scenario, this stage of the variability (e.g., when Spitzer 4.5 μm secondary eclipse depth was at its lowest) was observed in 2012. The photometric precision of the MOST 2012 light curve alone is not sufficient to set a meaningful constraint on A_g for that year. Nevertheless, our global constraint of $A_g < 0.47$ (averaged over all five MOST light curves) rules out most of the 0.4 - 1.0 range, and tentatively suggests that the model proposed by Tamburo et al. (2018) may not explain the observed 4.5 μm secondary eclipse variability. Ultimately, high-precision observations with the upcoming CHAracterising ExOPlanet Satellite (CHEOPS) space telescope (Broeg et al. 2013) would provide improved constraints on, and possibly an actual determination of, the albedo of 55 Cnc e.

6.2. Possible origins of the phase modulations

In this study, we analyzed five sequences of MOST data of 55 Cnc e obtained between 2011 and 2015 and searched for photometric modulation in phase with the period of planet e. We assumed a modulation that was periodic and estimated its parameters (amplitude and phase) for the five individual light curves. We detected a phase modulation and find that it is variable from year to year. Intriguingly, the amplitude of this modulation in flux is too large to be due to scattered light from the planet. We note that our measurements of the phase amplitude are also higher than the predictions by Kane et al. (2011) who assumed various scenarios for the planet; the most optimistic is that of a lava world with a modulation amplitude < 20 ppm. Consequently, the observed modulation must have a different origin.

6.2.1. Instrumental origin

First, it has been proposed by W11 that the variation may be due to instrumental noise. To verify this, we analyzed the light curve of the nearby star 53 Cnc, a bright giant star falling on the MOST CCD during the observations of 55 Cnc. We applied the same detrending procedures to the light curves of 53 Cnc and do not find any flux modulation at the timescale of the orbital period of 55 Cnc e. While we are pretty confident that the modulation observed in the 55 Cnc is not due to instrumental artifacts, this has to be confirmed by other long-term observations in the optical wavelength range. Assuming this modulation is indeed related to the 55 Cnc system, we can invoke multiple hypothetical physical scenarios to explain its origin.

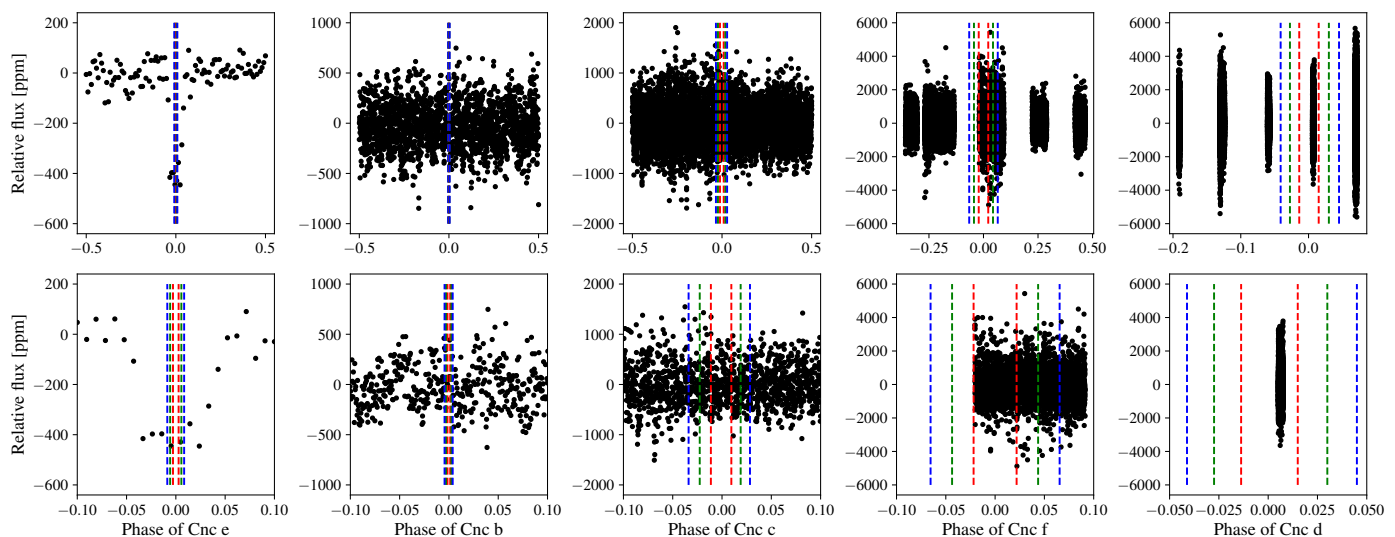


Fig. 9. From left to right: Light curves binned into 5-min intervals, phase folded at the orbital period of planet e, b, c, f, and d. The vertical lines indicate the 1, 2, and 3σ uncertainties of the time of mid-transit (red, green, and blue, respectively). The bottom panels are zoomed-in views of the mid-time transit event for each planet.

6.2.2. Stellar variability

We considered the possibility of variability of the star as the source of the phase modulation signal. The rotation period of 55 Cnc A is ~ 40 days and the lifetime of star spots on solar-type stars ranges from 10 to 350 days (Namekata et al. 2019). These timescales are too long for spot-related stellar variability to be the source of the signal. We also considered stellar pulsations, but in Sun-like stars p-mode oscillations have periods of just 5-10 minutes (Di Mauro 2016), which is much too short to be the source of the observed modulations at the period of 55 Cnc e. We conclude that neither star spots nor stellar pulsations can explain the 55 Cnc e phase modulation signal.

6.2.3. Star-planet interaction

As proposed by W11, this signal can be the signature of an interaction between the host star and planet e. For example, from ultraviolet observations Bourrier et al. (2018b) proposed that the interaction of the planet with the stellar magnetic field inside the corona might trigger coronal rain. The material would be accreted onto the star along the magnetic field lines, and cool and emit at optical wavelengths (see discussion in Sec. 4.3 of Bourrier et al. 2018b). In this scenario, the variability in the observed modulation would be due to the variability of the stellar corona with time and to exchanges of variable amounts of material over time. To validate this scenario, we looked for modulations of the H- α stellar activity indicator obtained over the last ≈ 20 years (Bourrier et al. 2018a) in phase with the planetary orbital period, but without success (see Fig. 10). This may be because the sampling and time coverage may be too poor to access the presence of such a modulation at the level allowed by the data quality. However, it is also possible that the signal is smeared out by the variation in the phase offsets we observe in the modulation from year to year, which is on timescales much shorter than the whole data coverage, even possibly shorter than the stellar rotation period. For this reason, we considered the subseries of stellar activity indicator measurements that are temporally close to the MOST observations. Figure 10 shows that there is indeed

a similarity in the temporal behavior between the activity index and the amplitude of the flux modulation.

A supporting argument for the presence of star-planet interactions comes from the results of Folsom et al. (submitted), who employed spectropolarimetry to derive the strength and geometry of the stellar magnetic field. Their 3D stellar wind modeling based on the surface magnetic field map indicated that the orbit of the planet lies entirely inside the Alfvén surface of the stellar wind. This implies that the star and the planet are magnetically connected and that the planet could influence the stellar wind such that the interaction can reach the stellar surface. If this scenario is correct, the observed flux modulation could be evidence of plasma exchange through reconnecting magnetic field lines of the star and planet.

The interaction could then lead to the formation of a spot on the stellar surface that rotates in phase with the planetary orbital motion, hence unrelated to the stellar rotation period (Shkolnik et al. 2003; Strugarek et al. 2015). Such a scenario has already been proposed to explain the optical flux modulation observed for the τ Boo (Walker et al. 2008) and CoRoT-2 (Pagano et al. 2009) systems, as well as in X-rays for HD 17156 (Maggio et al. 2015). If a spot is present, calculations done for hot Jupiters have shown that the activity should be phased with the planetary orbital period and present a phase offset (Lanza 2012) similar to what was recently detected by Cauley et al. (2018). Assuming this argument also holds for systems hosting lower mass planets and the quality and sampling of the data is high enough, the interaction should be detectable by analyzing the temporal behavior of magnetic activity indicators (Strugarek et al. 2019). Our results shown in Fig. 10 suggest that the interaction may indeed be detectable with simultaneous photometric and spectroscopic high-quality observations, the former covering the whole planet orbital period and the latter covering multiple activity indicators.

6.2.4. Transiting circumstellar dust torus

Alternatively, the phase modulation in flux could be the signature of a transiting circumstellar dust torus. This dust cloud could also exchange material with the planet itself, which might originate from volcanism at the surface of 55 Cnc e (analogous to Io's cold

plasma torus; Krüger et al. 2003). The density and optical depth of the torus changes over time. Thus, both the transit depth and flux modulation vary (see Fig. 12). This scenario would be in line with the variability observed in the IR secondary eclipse depth (Demory et al. 2016b; Tamburo et al. 2018). Moreover, if the material of this torus indeed originates from the planet, it could be alimented from material (typically dust) inside the planetary Roche lobe ($\sim 4.94 - 5.22 R_{\oplus}$), which itself is highly irradiated and subject to intense tidal forces. In this paradigm, the proportion of scattered light also depends on the spatial distribution of the dust inside the Roche lobe and the position of the planet along its orbit. If the distribution of scattering material material evolved, the phase curve would as well.

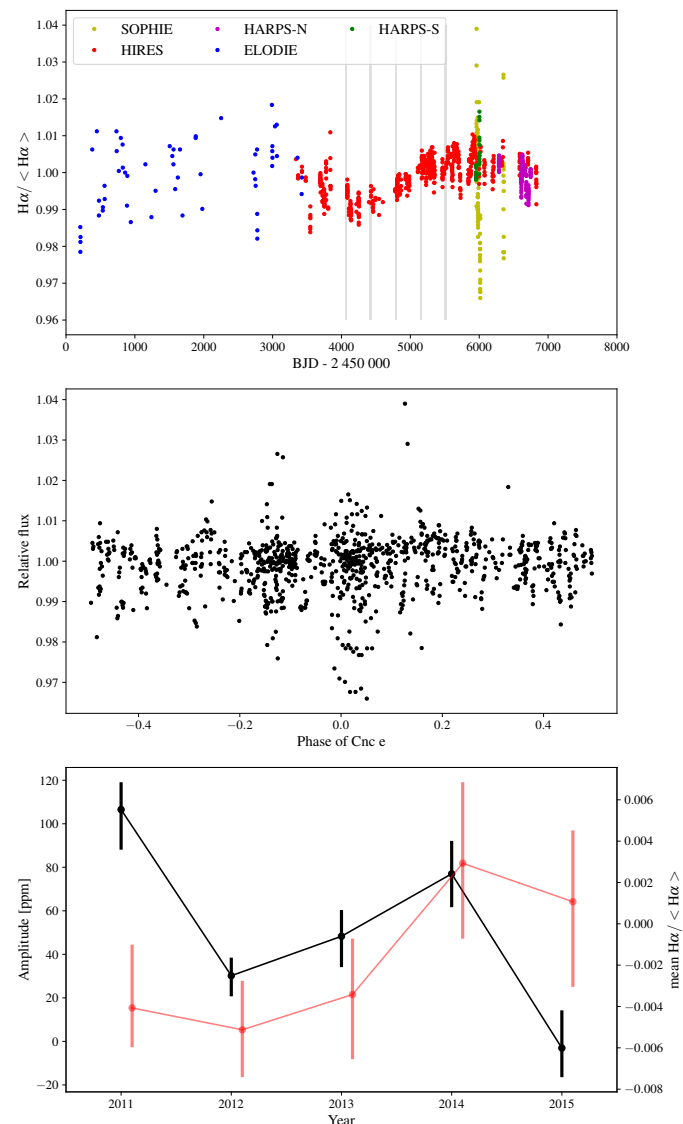


Fig. 10. Top: H- α activity index of the 55 Cnc A star (see Fig. 2 of Bourrier et al. 2018a, second panel) and MOST observations dates (gray). Middle: Combined H- α data phase folded at the planet orbital period. Bottom: Amplitudes of the modulation (see Table. 4) measured on MOST observations (black, left y-axis) and mean values of the H- α stellar activity indicator (red, right y-axis) evaluated around dates close to the MOST observations. The error bars on the mean H- α values are taken as the minimum and maximum values of the index in the considered year. We note the H- α values have been slightly shifted in time for visibility. We observe the increase/decrease of the modulation in phase with the increase/decrease of the stellar activity indicator.

6.3. Search for temporal variations in the transit parameters of 55 Cnc e

By independently analyzing the five light curves taken from 2011 to 2015, we observe some variations of the transit parameters from year to year. This is shown in Fig. 11 for the transit and modulation parameters. We observe a variability in the transit depth that seems in agreement with Demory et al. (2016b) and Bourrier et al. (2018a), who suggest variations over timescales of days or weeks. This is shown in Fig. 12 (reproduction of Fig. 15 of Bourrier et al. 2018a with our measurements added). However, while we measure a maximum deviation of the transit depth up to 40 ppm, all the measurements are within the 1σ values of each other (see Fig. 11). Hence, the transit depth variability is not beyond the expected statistical fluctuations of our MOST observations.

In Fig. 11, we also compare values obtained before and after the stray-light correction procedures (see Sec. 3.2). As expected, we observe that the stray-light correction improves the precision and even the accuracy of the transit parameters (see top panels), and by extension, the constraint on the eclipse depth. However, the impact on the inferred parameters of the modulation is less pronounced (see bottom panels).

7. Conclusions

We analyzed five sequences of MOST observations spanning several weeks of observations taken between 2011 and 2015. We carried out a careful reduction of the raw light curves following current MOST reduction techniques. In addition, we developed a new method, based on the cross-correlation of shorter subsequences to improve the correction of the stray-light noise.

We performed MCMC analyses of the combined detrended MOST light curves and derived the transit, secondary-eclipse, and phase-modulation parameters. We find transit parameters that are consistent with the most recent values given in Bourrier et al. (2018a). The secondary eclipse remains undetected in the MOST observations, but it allows us to constrain the albedo of 55 Cnc e to an upper limit of 0.47. We confirm the detection of the optical modulation in flux discovered by Winn et al. (2011) at the planet period and detect it at four additional epochs. Intriguingly, we find that its amplitude and phase are variable. At this point, we can only speculate about the origin of the effect. Simultaneous observations at various wavelengths could help to distinguish the origin of this variability that may be linked to the observed modulation observed in far-ultraviolet (Bourrier et al. 2018b) and IR wavelengths (Demory et al. 2016b; Tamburo et al. 2018). We argue that additional observations in the optical with Transiting Exoplanet Survey Satellite (TESS, Ricker et al. 2014) and CHEOPS will be extremely valuable for our understanding of this mysterious planet. Finally, we do not detect any transit for planets b, c, f, and d in the MOST observations.

Acknowledgements. S. Sulis, M. Lendl, P. Cubillos, and L. Fossati acknowledge support from the Austrian Research Promotion Agency (FFG) under project 859724 “GRAPPA”. D. Dragomir acknowledges support provided by NASA through Hubble Fellowship grant HSTHF2-51372.001-A awarded by the Space Telescope Science Institute, which is operated by the Association of Universities for Research in Astronomy, Inc., for NASA, under contract NAS5-26555. V. Bourrier acknowledges support by the Swiss National Science Foundation (SNSF) in the frame of the National Centre for Competence in Research PlanetS, and has received funding from the European Research Council (ERC) under the European Union’s Horizon 2020 research and innovation programme (project Four Aces; grant agreement No 724427). The authors thank Apurva Oza for a careful reading of an earlier version of the manuscript and the anonymous referee for his/her very useful comments.

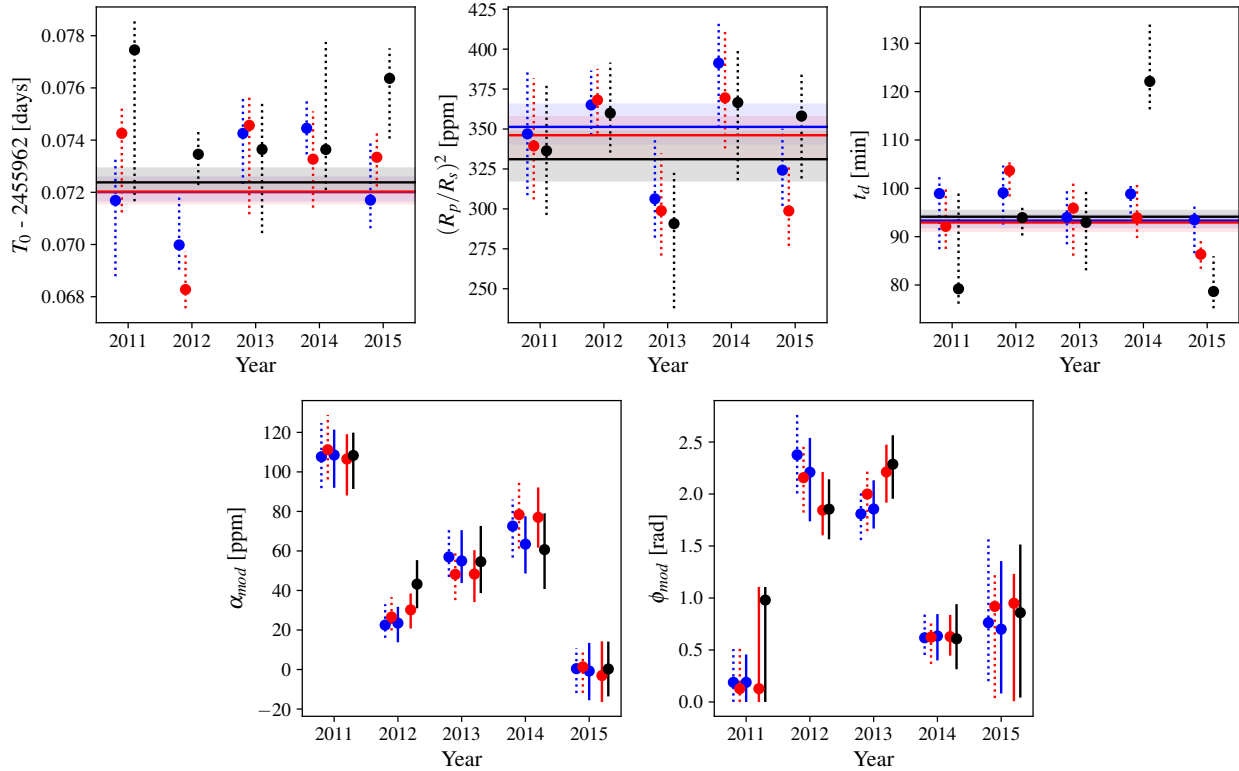


Fig. 11. From left to right: Estimated parameters of the 55 Cnc e transit (T_0 , $(R_p/R_s)^2$, t_d) and of the modulation in flux (α_{mod} and ϕ_{mod}). In all panels, dotted points indicate the best-fitting values derived from each of the 5 MOST data analyzed separately using the classical and time-shift detrending procedures and values obtained using the light curve not corrected for the stray-light systematics (i.e., resulting only from the pre-whitening step; see Sec. 3.1). In the three first panels, the horizontal solid lines represent the values derived from the combined light curves (see Table 3 and Sec. 4.1) with their 1σ uncertainties (shaded area). In the two last panels, the solid points represent the modulation parameters derived during the analysis of these combined light curves (see Table 4 and Sec. 4.2).

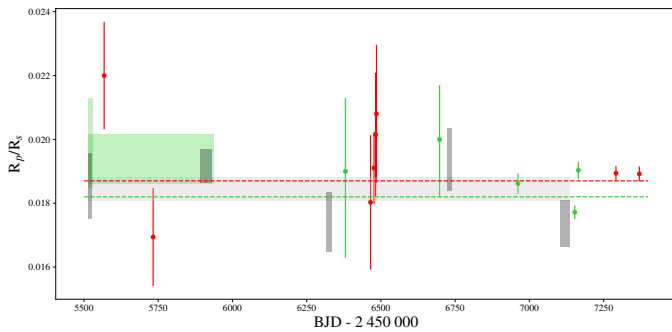


Fig. 12. Reproduction of Fig. 15 of Bourrier et al. (2018a) representing the planet-to-star radius ratio measured over time with various instruments. Observations in the optical are shown in green. Chronologically, we show values from Gillon et al. (2012) and D14 with MOST; from de Mooij et al. (2014) with Alhambra Faint Object Spectrograph and Camera (ALFOSC) and from Bourrier et al. (2018a) with the Space Telescope Imaging Spectrograph (STIS) spectrograph onboard the Hubble Space Telescope (HST). Our measurements derived from MOST and resulting from the time-shift procedure are shown in black (individual points and combined light curves). Observations in IR are represented in red: Demory et al. (2016a) with Spitzer and Tsiaras et al. (2016) with Wide Field Camera 3 (WFC3) onboard HST. Following Bourrier et al. (2018a), the dashed green line shows the value obtained from the fit to the three combined STIS visits and the dashed red line shows the value obtained from the fit to the combined Spitzer visits (Demory et al. 2016b). The values represented by rectangles indicate radius ratios that have been estimated over an extended period of time.

References

- Adams, E. R., Seager, S., & Elkins-Tanton, L. 2008, *ApJ*, 673, 1160
 Angelo, I. & Hu, R. 2017, *AJ*, 154, 232
 Angerhausen, D., DeLarme, E., & Morse, J. A. 2015, *PASP*, 127, 1113
 Batalha, N. M., Borucki, W. J., Bryson, S. T., et al. 2011, *ApJ*, 729, 27
 Batygin, K. & Laughlin, G. 2015, *Proceedings of the National Academy of Science*, 112, 4214
 Bourrier, V., Dumusque, X., Dorn, C., et al. 2018a, *A&A*, 619, A1
 Bourrier, V., Ehrenreich, D., Lecavelier des Etangs, A., et al. 2018b, *A&A*, 615, A117
 Broeg, C., Fortier, A., Ehrenreich, D., et al. 2013, in *European Physical Journal Web of Conferences*, Vol. 47, *European Physical Journal Web of Conferences*, 03005
 Cauley, P. W., Shkolnik, E. L., Llama, J., Bourrier, V., & Moutou, C. 2018, *AJ*, 156, 262
 Chiang, E. & Laughlin, G. 2013, *MNRAS*, 431, 3444
 Crossfield, I. J. M. 2012, *A&A*, 545, A97
 Cubillos, P., Harrington, J., Lored, T. J., et al. 2017, *AJ*, 153, 3
 Davis, T. A. & Wheatley, P. J. 2009, *MNRAS*, 396, 1012
 Dawson, R. I. & Fabrycky, D. C. 2010, *ApJ*, 722, 937
 de Mooij, E. J. W., López-Morales, M., Karjalainen, R., Hrudkova, M., & Jayawardhana, R. 2014, *ApJ*, 797, L21
 Demory, B.-O. 2014, *ApJ*, 789, L20
 Demory, B.-O., Gillon, M., de Wit, J., et al. 2016a, *Nature*, 532, 207
 Demory, B.-O., Gillon, M., Deming, D., et al. 2011a, *A&A*, 533, A114
 Demory, B.-O., Gillon, M., Madhusudhan, N., & Queloz, D. 2016b, *MNRAS*, 455, 2018
 Demory, B.-O., Seager, S., Madhusudhan, N., et al. 2011b, *ApJ*, 735, L12
 Di Mauro, M. P. 2016, in *Frontier Research in Astrophysics II*, 29
 Dorn, C., Harrison, J. H. D., Bonsor, A., & Hands, T. O. 2018, *MNRAS*, 484, 712
 Dragomir, D., Matthews, J. M., Eastman, J. D., et al. 2013, *ApJ*, 772, L2
 Dragomir, D., Matthews, J. M., Winn, J. N., & Rowe, J. F. 2014, in *IAU Symposium*, Vol. 293, *IAU Symposium*, ed. N. Haghighipour, 52–57
 Ehrenreich, D., Bourrier, V., Bonfils, X., et al. 2012, *A&A*, 547, A18

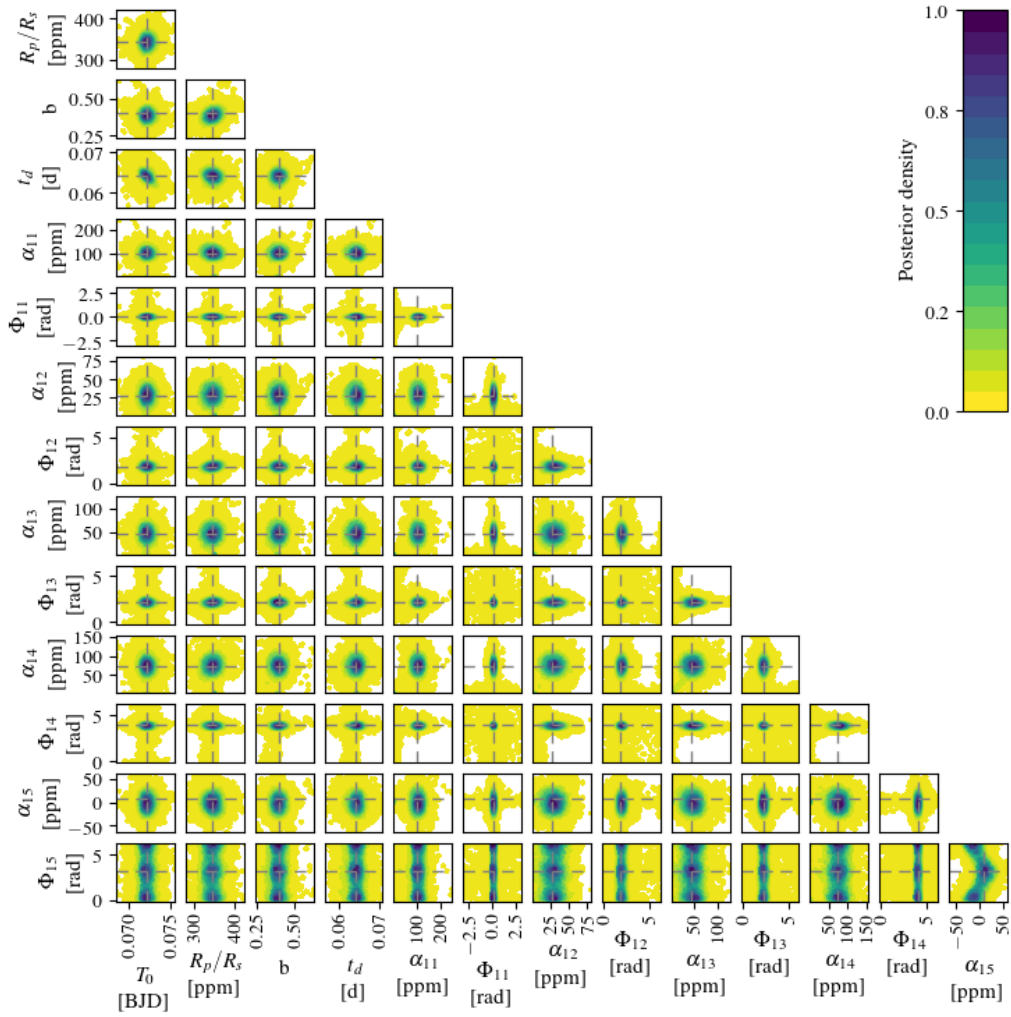


Fig. 13. Pairwise marginal posteriors of the MCMC analysis for the 55 Cnc e planet and the phase variation modeled as described in (1). For visibility, we plot $T_0 - 4417$ and fold the Φ_{11} parameter over $\pm\pi$. We found a double maxima for the Φ_{15} parameter around 0 [mod 2π] and π , which is meaningless as the corresponding modulation amplitude α_{15} is roughly null.

Ehrenreich, D. & Désert, J.-M. 2011, *A&A*, 529, A136
Esteves, L. J., De Mooij, E. J. W., & Jayawardhana, R. 2015, *ApJ*, 804, 150
Fischer, D. A., Marcy, G. W., Butler, R. P., et al. 2008, *ApJ*, 675, 790
Folsom, C. P., Fionnagáin, D. O., Fossati, L., et al. submitted
Fressin, F., Torres, G., Charbonneau, D., et al. 2013, *ApJ*, 766, 81
Fulton, B. J. & Petigura, E. A. 2018, *AJ*, 156, 264
Fulton, B. J., Petigura, E. A., Howard, A. W., et al. 2017, *AJ*, 154, 109
Gandolfi, D., Barragán, O., Livingston, J. H., et al. 2018, *A&A*, 619, L10
Gillon, M., Demory, B.-O., Benneke, B., et al. 2012, *A&A*, 539, A28
Gillon, M., Lanotte, A. A., Barman, T., et al. 2010, *A&A*, 511, A3
Hansen, B. M. S. & Murray, N. 2012, *ApJ*, 751, 158
Jansen, T. & Kipping, D. 2018, *MNRAS*, 478, 3025
Jin, S. & Mordasini, C. 2018, *ApJ*, 853, 163
Jones, H. R. A., Paul Butler, R., Tinney, C. G., et al. 2002, *MNRAS*, 333, 871
Kane, S. R., Gelino, D. M., Ciardi, D. R., Dragomir, D., & von Braun, K. 2011, *ApJ*, 740, 61
Kane, S. R., Wittenmyer, R. A., Hinkel, N. R., et al. 2016, *ApJ*, 821, 65
Kite, E. S., Fegley, Jr., B., Schaefer, L., & Gaidos, E. 2016, *ApJ*, 828, 80
Krüger, H., Geissler, P., Horányi, M., et al. 2003, *Geophys. Res. Lett.*, 30, 2101
Kubyskhina, D., Fossati, L., Erkaev, N. V., et al. 2018, *A&A*, 619, A151
Lanza, A. F. 2012, *A&A*, 544, A23
Lecavelier des Etangs, A. 2007, *A&A*, 461, 1185
Lendl, M., Cubillos, P. E., Hagelberg, J., et al. 2017, *A&A*, 606, A18
Maggio, A., Pillitteri, I., Scandariato, G., et al. 2015, *ApJ*, 811, L2
Mandel, K. & Agol, E. 2002, *ApJ*, 580, L171
Matthews, J. M. 2004, in *BAAS*, Vol. 36, AAS Meeting Abstracts, 1563

Mayor, M., Marmier, M., Lovis, C., et al. 2011, arXiv e-prints, arXiv:1109.2497
Miguel, Y. 2019, *MNRAS*, 482, 2893
Mordasini, C., Alibert, Y., Georgy, C., et al. 2012, *A&A*, 547, A112
Motalebi, F., Udry, S., Gillon, M., et al. 2015, *A&A*, 584, A72
Namekata, K., Maehara, H., Notsu, Y., et al. 2019, *ApJ*, 871, 187
Owen, J. E. & Wu, Y. 2017, *ApJ*, 847, 29
Pagano, I., Lanza, A. F., Leto, G., et al. 2009, *Earth Moon and Planets*, 105, 373
Petigura, E. A., Howard, A. W., & Marcy, G. W. 2013, *Proceedings of the National Academy of Science*, 110, 19273
Pont, F., Zucker, S., & Queloz, D. 2006, *MNRAS*, 373, 231
Poppenhaeger, K. & Schmitt, J. H. M. M. 2011, *ApJ*, 735, 59
Ricker, G. R., Winn, J. N., Vanderspek, R., et al. 2014, in *Society of Photo-Optical Instrumentation Engineers (SPIE) Conference Series*, Vol. 9143, Proc. SPIE, 914320
Ridden-Harper, A. R., Snellen, I. A. G., Keller, C. U., et al. 2016, *A&A*, 593, A129
Rogers, L. A., Bodenheimer, P., Lissauer, J. J., & Seager, S. 2011, *ApJ*, 738, 59
Rogers, L. A. & Seager, S. 2010, *ApJ*, 712, 974
Rouan, D., Deeg, H. J., Demangeon, O., et al. 2011, *ApJ*, 741, L30
Rowe, J. F., Matthews, J. M., Seager, S., et al. 2006, *ApJ*, 646, 1241
Rowe, J. F., Matthews, J. M., Seager, S., et al. 2008, *ApJ*, 689, 1345
Rucinski, S. M. et al. 2004, *PASP*, 116, 1093
Savitzky, A. & Golay, M. J. E. 1964, *Analytical Chemistry*, 36, 1627
Sheets, H. A. & Deming, D. 2017, *AJ*, 154, 160
Shkolnik, E., Walker, G. A. H., & Bohlender, D. A. 2003, *ApJ*, 597, 1092
Shkolnik, E. L. & Llama, J. 2018, *Signatures of Star-Planet Interactions*, 20

- Strugarek, A., Brun, A. S., Donati, J. F., Moutou, C., & Réville, V. 2019, arXiv e-prints, arXiv:1907.01020
- Strugarek, A., Brun, A. S., Matt, S. P., & Réville, V. 2015, *ApJ*, 815, 111
- Tamburo, P., Mandell, A., Deming, D., & Garhart, E. 2018, *AJ*, 155, 221
- Tsiaras, A., Rocchetto, M., Waldmann, I. P., et al. 2016, *AJ*, 820, 99
- Van Eylen, V., Agentoft, C., Lundkvist, M. S., et al. 2018, *MNRAS*, 479, 4786
- Vogt, S. S., Burt, J., Meschiari, S., et al. 2015, *ApJ*, 814, 12
- von Braun, K., Boyajian, T. S., ten Brummelaar, T. A., et al. 2011, *ApJ*, 740, 49
- Walker, G., Matthews, J., Kuschnig, R., et al. 2003, *PASP*, 115, 1023
- Walker, G. A. H., Croll, B., Matthews, J. M., et al. 2008, *A&A*, 482, 691
- Winn, J. N., Holman, M. J., Torres, G., et al. 2008, *ApJ*, 683, 1076
- Winn, J. N., Matthews, J. M., Dawson, R. I., et al. 2011, *ApJ*, 737, L18
- Wright, J. T. & Miller, B. 2015, in *IAU General Assembly*, Vol. 29, 2258453
- Yee, S. W., Petigura, E. A., & von Braun, K. 2017, *ApJ*, 836, 77

Appendix A: Long-term variability affecting the 55 Cancri light curve: Signature of the stellar activity

During the pre-whitening stage (see Sec. 3.1), we observe a long-term variation in each of the light curves. This variation is shown in Fig. A.1. We observe variations over timescales close to half of the stellar rotation period ($38.8/2$ day) but that changes in both amplitude and phase from year to year (see right column). When binning the observations into two-hour intervals (see left column), we measure a dispersion around the mean value of 656, 1471, 1116, 774, and 1733 ppm for the 2011 to 2015 datasets, respectively. We attribute these variations to the evolution of the stellar activity as they are not strictly increasing as would be expected in case of instrumental systematics. We note that the stray-light systematics discussed in Sec. 3.2 are clearly visible in the three first datasets. Correcting for the long-term variation before correcting the stray-light systematics, as done in this study contrary to previous studies of W11 and D14, avoids the introduction of an offset between the one-day sequences used in the analysis described in Sec. 3.2.

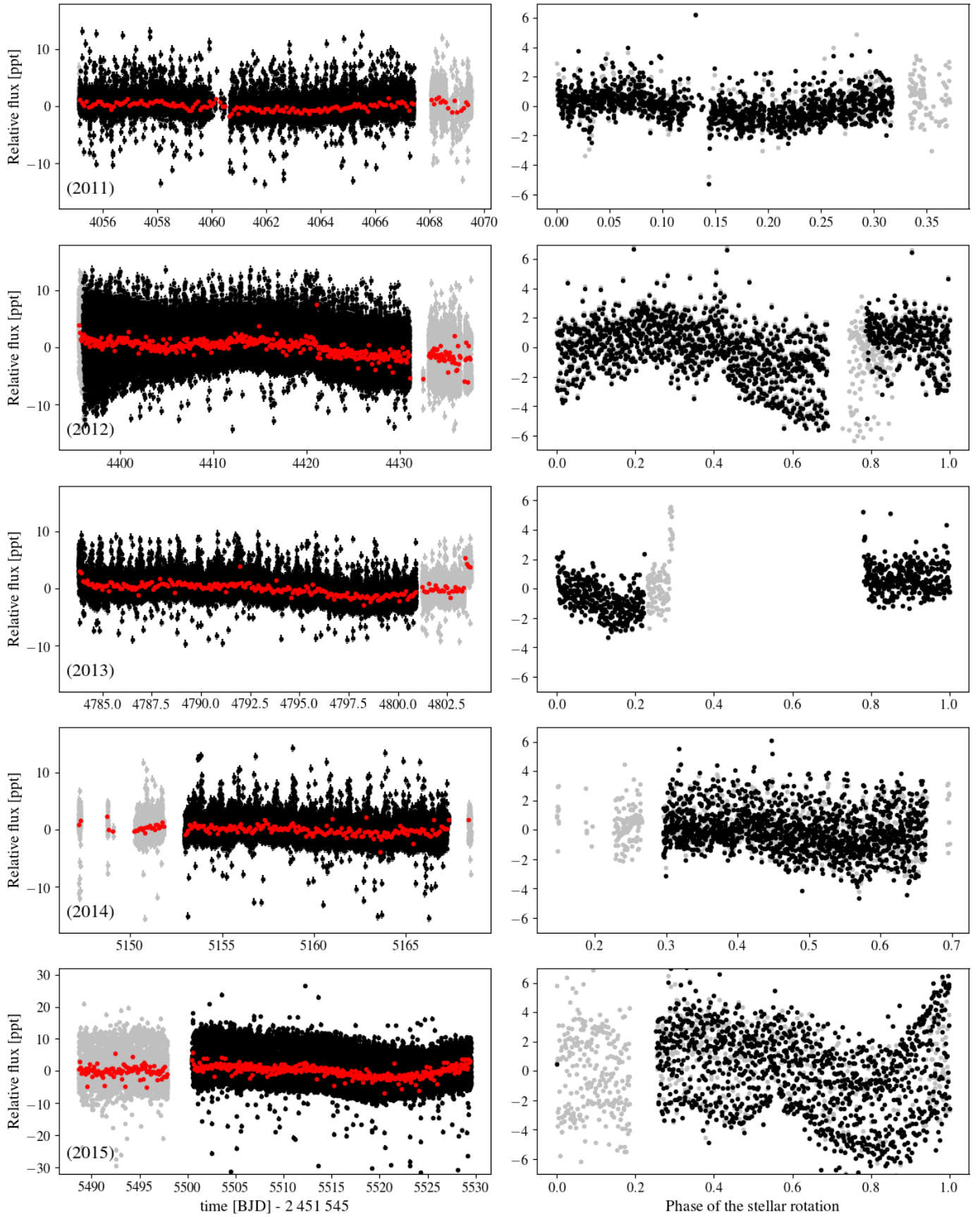


Fig. A.1. From top to bottom: Light curves taken in 2011, 2012, 2013, 2014, and 2015 obtained before the long-term variation correction in the pre-whitening stage (see Sec. 3.1). The y-axis is in part-per-thousand. The removed sections of the light curves are shown in gray. The left column panels represent the light curve as a function of time. The long-term variation is well observed on the data binned at two-hour intervals (red). The right column panels represent these flux phase folded at the stellar rotation period of 38.8 days (binned into 30-min intervals). We note the different scale on the y-axis of the 2015 plot on the bottom.